Doctoral network for microprocess engineering for electrosynthesis

DELIVERABLE REPORT

Deliverable no. / title:	D1.1 Continuum-scale flow cell model published including open-source code
Lead beneficiary:	11DC-ZHA
Nature of deliverable:	OTHER
Dissemination level:	PU - Public
Due date:	February 2025 (month 26)
Grant Agreement number:	101073003
Project acronym:	MiEl
Project title:	Doctoral network for microprocess engineering for electrosynthesis - new synthesis concepts for the pharmaceutical/ fine chemical industry
Funding scheme:	Marie Skłodowska-Curie Doctoral Networks HORIZON-MSCA-2021-DN-01
Coordinator:	Fraunhofer ICT Dr. Julia Melke **Tel:** 0049 721 4640 547 **E-mail:** julia.melke@ict.fraunhofer.de
Project website:	https://project-miel.eu/
Disclaimer:	Funded by the European Union. Views and opinions expressed are however those of the author(s) only and do not necessarily reflect those of the European Union. Neither the European Union nor the granting authority can be held responsible for them.

Table of content

List of symbols

Roman characters

c	Local concentration $[\mathrm{mol/m^3}]$	Re	Reynolds number
d	Diameter $[\mathrm{m}]$	s	Interelectrode gap $[\mathrm{m}]$
D	Diffusion coefficient $[\mathrm{m^2/s}]$	t	Time $[\mathrm{s}]$
E	Electrode potential $[\mathrm{V}]$	T	Temperature $[\mathrm{K}]$
F	Faraday constant, $96{,}485\ \mathrm{C/mol}$	u	Ionic mobility $[\mathrm{m^2 mol/J \cdot s}]$
i	Current density $[\mathrm{A/m^2}]$	$\bar{u}$	Average velocity $[\mathrm{m/s}]$
I	Identity matrix	u	Local velocity $[\mathrm{m/s}]$
J	Molar flux density $[\mathrm{mol/m^2 \cdot s}]$	U	Flow cell potential difference $[\mathrm{V}]$
k	Kinetic constant $[\mathrm{m/s}]$ (or $[\mathrm{s^{-1}}]$)	v	CV scan rate $[\mathrm{V/s}]$
L	1D domain length, or 2D cell length $[\mathrm{m}]$	w	Flow cell width $[\mathrm{m}]$
N	Molar flux density with convection $[\mathrm{mol/m^2 \cdot s}]$	x	Distance in 1D domain, or axial coordinate in electrode length $[\mathrm{m}]$
p	Local pressure $[\mathrm{Pa}]$	y	Axial coordinate along the interelectrode gap $[\mathrm{m}]$
R	Bulk chemical reaction rate $[\mathrm{mol/m^3 \cdot s}]$	z	Charge number of ionic species
R	Universal gas constant, $8.314\ \mathrm{J/mol \cdot K}$		

Greek characters

α	Cathodic charge transfer coefficient	Λ	Dimensionless electrochemical rate constant
δ	Nernst linear diffusion layer $[\mathrm{m}]$	μ	Dynamic fluid viscosity $[\mathrm{Pa \cdot s}]$
ε	Artificial concentration $[\mathrm{mol/m^3}]$	ν	Stoichiometric coefficient
η	Overpotential $[\mathrm{V}]$	ρ	Fluid density $[\mathrm{kg/m^3}]$
κ	Local solution conductivity $[\mathrm{S/m}]$	ϕ	Local potential $[\mathrm{V}]$
λ	Dimensionless chemical rate constant		

Subscripts and superscripts

a	Anodic	lim	Limiting
act	Activation	loc	Local, as evaluated at the interface
avg	Average	max	Maximum
bulk	Bulk	OCV	Open circuit voltage
c	Cathodic	ohmic	Ohmic
cell	Cell	out	Outlet
conc	Concentration	p	Peak
e	Electron	ref	Reference
eq	Equilibrium	s	At electrode
f	Formal	T	Transpose
h	Hydrodynamic	v	Switching
i	Referred to the i-th species	w	At the wall/interface
in	Inlet	WE	Working electrode
j	Referred to the j-th species	0	Standard
l	At solution	$*$	Dimensionless

Other characters

∇ Nabla operator

∂ Partial derivative

1. Introduction

Contrary to most traditional methods, electrochemical synthesis provides a greener, safer and more atom efficient alternative to reaction pathways towards useful compounds [1]. In the field of organic synthesis, chemists are now resorting to electrochemistry to achieve novel reactivities and enhanced selectivity, thus avoiding toxic chemicals via potential-induced electron transfer instead [2]. However, main reaction pathways are not always fully known, calling for dynamic electroanalytical techniques such as Cyclic Voltammetry (CV) to assess the current-potential curves that evidence the kinetics and mechanism involved [3]. Moreover, dealing with complex processes such as multi-electron transfer with coupled homogeneous chemical reactions may require computational modelling to comprehend and interpret competing interactions as they relate to mass transport, whether in batch or in flow.

Considering this, the main objective established for this deliverable was to develop a 2D continuum scale flow cell model via COMSOL Multiphysics v. 6.2 [4] which could serve as the modelling basis and proof-of-concept for further collaborative work within the MiEl network. In order to conceive a model with acceptable complexity, the ideal scenario was to approach a dummy, multi-step electroorganic synthesis with physically meaningful parameters and no adsorption, as defined below. The adopted nomenclature for the reaction mechanisms is that of Testa-Reinmuth, in which "E" represents an electrochemical process, while "C" a chemical step [5], here considered first-order and irreversible.

Anodic reaction (EEC):

E: $\mathrm{A} \rightleftharpoons \mathrm{B}^{+} + \mathrm{e}^{-}, \ \ (E^{0}_{\mathrm{f,a},1}, k^{0}_{\mathrm{a},1}, \alpha_{\mathrm{a},1})$

E: $\mathrm{B}^{+} \rightleftharpoons \mathrm{C}^{2+} + \mathrm{e}^{-}, \ \ (E^{0}_{\mathrm{f,a},2}, k^{0}_{\mathrm{a},2}, \alpha_{\mathrm{a},2})$

C: $\mathrm{C}^{2+} \rightarrow \mathrm{D}^{2+}, \ \ (k_{\mathrm{f,a}})$

Cathodic reaction (ECE):

E: $\mathrm{X} + \mathrm{e}^{-} \rightleftharpoons \mathrm{Y}^{-}, \ \ (E^{0}_{\mathrm{f,c},1}, k^{0}_{\mathrm{c},1}, \alpha_{\mathrm{c},1})$

C: $\mathrm{Y}^{-} \rightarrow \mathrm{Z}^{-}, \ \ (k_{\mathrm{f,c}})$

E: $\mathrm{Z}^{-} + \mathrm{e}^{-} \rightleftharpoons \mathrm{W}^{2-}, \ \ (E^{0}_{\mathrm{f,c},2}, k^{0}_{\mathrm{c},2}, \alpha_{\mathrm{c},2})$

As opposed to adapting an experimental case from the literature, the decision to develop a dummy synthesis scenario was informed by an intention to first focus on the effect of the kinetic parameters upon the reactions' electroanalytical voltametric responses in CV. Such route also enabled a conception of complex multi-step electron transfers that allow for a greater understanding of the continuum scale modelling capabilities at hand. Given this, the subsequent work is divided in two sections: the first concerns the 1D CV modelling of the reactions themselves, while the second adopts said results to the context of flow cell operation.

2. 1D Cyclic Voltammetry Model

Cyclic voltammetry is an electroanalytical technique amply used for the study of redox reactions, enabling valuable insight on the reaction mechanism of a given system and its kinetics [6]. By applying a time-dependent potential ramp to the working electrode (WE), the resulting current response reveals crucial characteristics of the reaction, such as electron transfer rates, chemical reactions, and kinetic limitations when set against diffusion of the species [6]. However, given the complexity of mechanisms involving multi-electron transfer, the interpretation of experimental voltammograms can be facilitated by numerical simulations [7]. Indeed, by combining experimental CV data with mathematical modelling, one can better understand the involved kinetics, and optimize the electrochemical systems themselves [6].

As in this work, CV models often assume isothermal conditions and homogeneous initial concentrations for both the reactants and the intermediate species, as well as an inert supporting electrolyte [7]. These and other necessary assumptions are cleared in the following section, detailing the construction of a 1D CV model meant for the study of the anodic (EEC) and cathodic (ECE) reactions.

2.1. Constitutive Equations

The first variable to define when modelling cyclic voltammetry is the WE potential itself, with respect to a reference, swiped along the duration of the electroanalytical experiment. It is thus characterized by the switching potentials E_{v1} and E_{v2} $[\mathrm{V}]$, defining the extremities of the sweep, and the constant scan rate v $[\mathrm{V/s}]$, determining its overall velocity. Consequently, the total time of a cycle $t_{\max}$ $[s]$ is then:

$$t_{\max} = \frac{2|E_{\mathrm{v1}} - E_{\mathrm{v2}}|}{v} \qquad \text{(Eq. 2.1)}$$

with the time-dependent potential itself being then defined as:

$$E(t) = \phi_{\mathrm{s}}(t) - \phi_{\mathrm{l}}(t) = \begin{cases} E_{\mathrm{v1}} + vt & \text{if } \ 0 \le t < \dfrac{t_{\max}}{2} \\ E_{\mathrm{v2}} - vt & \text{if } \ \dfrac{t_{\max}}{2} < t \le t_{\max} \end{cases} \qquad \text{(Eq. 2.2)}$$

The total CV time for one cycle as defined in Eq. 2.1 is of special importance, since it enables the estimation of the maximum Nernst linear diffusion layer's thickness δ (Fig. 2.1) of a given species. As the diffusion coefficient D $[\mathrm{m^2/s}]$ is assumed equal for all involved species, the computation of δ allows for the definition of an appropriate distance L $[\mathrm{m}]$ away from the WE, for which to define the bulk boundary:

$$L = 6\delta \Leftrightarrow L = 6\sqrt{D t_{\max}} \qquad \text{(Eq. 2.3)}$$

As observed, the dependence of L on $t_{\max}$ directly relates the bulk boundary's distance from the WE as being defined by the CV's operating conditions (E_{v1}, E_{v2} and v, as per Eq. 2.2). Moreover, the computation of an appropriate L has to be such that it is significantly small when compared with the round WE's electroactive surface area, so that a 1D modelling approach is assumed along the x axis (Fig. 2.1) [7], defining the overall domain as $x = [0, L]$.

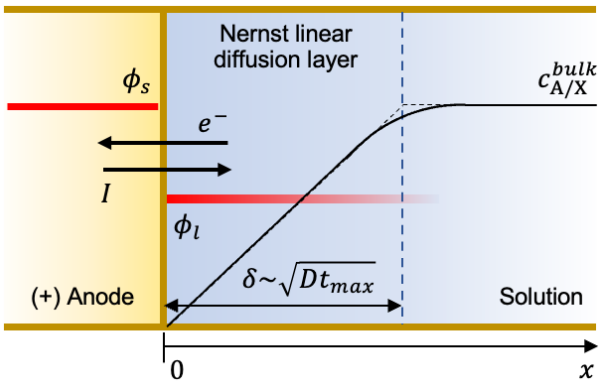

Figure 2.1: Schematic of the 1D CV modelling domain, here depicted in 2D, for the anodic case (EEC). It evidences: the definition of the Nernst linear diffusion layer δ; the bulk concentration of reactant species A or X; and the electrostatic potential drop (from ϕ_s to ϕ_l) that takes place at the surface ($x = 0$), via the formation of the double layer and the electrochemical reaction itself.

Consequently, regarding mass transport, assuming the species to be diluted in an unstirred solution, the molar flux $\mathbf{J}_i$ $[\mathrm{mol/m^2 \cdot s}]$ of charged particles by diffusion and electrostatic forces is dictated by the Nernst-Planck equation:

$$\mathbf{J}_i = -D_i \nabla c_i - z_i u_i F c_i \nabla \phi_l \qquad \text{(Eq. 2.4)}$$

in which the latter term represents the migrative flux as it relates to the species charge number z_i, its ionic mobility u_i $[\mathrm{m^2 mol/J \cdot s}]$, concentration c_i and the solution's electric field $\nabla\phi_l$ $[\mathrm{V/m}]$. However, assuming the presence of a supporting electrolyte in excess, conferring a high conductivity to the whole solution and thus reducing ohmic losses, migration can be neglected, since the electrostatic potential gradient is considerably small. Such then simplifies Eq. 2.4 to Fick's first law of diffusion in one-dimension:

$$\mathbf{J}_i \approx -D_i \frac{\partial c_i}{\partial x} \qquad \text{(Eq. 2.5)}$$

With the definition of the molar flux as being fully influenced by diffusion, the formulation of the mass-balance of each species may then proceed thus:

$$\frac{\partial c_{\mathrm{i}}}{\partial t} + \nabla \cdot \mathbf{J}_{\mathrm{i}} = R_{\mathrm{i,j}} \Leftrightarrow \frac{\partial c_{\mathrm{i}}}{\partial t} = D_{\mathrm{i}} \frac{\partial^2 c_{\mathrm{i}}}{\partial x^2} + R_{\mathrm{i,j}} \quad \text{(Eq. 2.6)}$$

with $R_{\mathrm{i,j}}$ being the bulk homogeneous chemical reaction rate per unit volume $[\mathrm{mol/m^3 \cdot s}]$ of species i as it participates in a reaction j. The model is moreover dependent on the formulation of appropriate boundary conditions for the mass-balance equations. Given that the domain's maximum distance L from the electrode surface (Eq. 2.3) is sufficiently distant from the Nernst linear diffusion layer and encompasses the bulk solution, Dirichlet boundary conditions are applied. Thus, at $x = L$, each species' concentrations are specified as follows:

$$c_{\mathrm{A/X}}(L, t) = c_{\mathrm{A/X}}^{\mathrm{bulk}} \quad \text{(Eq. 2.7)}$$

$$c_{\mathrm{i}}(L, t) = 0 \quad \text{(Eq. 2.8)}$$

such that $\mathrm{A/X}$ refers to "either species A or X", while all intermediate species c_{i} are assumed to be non-existent at the bulk boundary (Eq. 2.8). As the concentrations are assumed homogeneous at $t = 0$, the initial values are also set as $c_{\mathrm{A/X}}(x, 0) = c_{\mathrm{A/X}}^{\mathrm{bulk}}$ and $c_{\mathrm{i}}(x, 0) = 0$. Concerning the electrode surface, however, the same does not apply, since concentrations are expected to vary as some species are produced/depleted via heterogeneous electrochemical reactions. Given this, Neumann boundary conditions are valid instead, such that for electroactive species:

$$-\mathbf{n} \cdot \mathbf{N}_{\mathrm{i}}|_{x=0} = \frac{-\nu_{\mathrm{i,j}} i_{\mathrm{loc,j}}(E(t))}{\nu_{\mathrm{e,j}} \mathrm{F}} \quad \text{(Eq. 2.9)}$$

i.e. as per Faraday's law of electrolysis, the normal component of the molar flux as evaluated at the electrode surface stands in direct relation to the time-variant partial local current density $i_{\mathrm{loc,j}}(t)$ $[\mathrm{A/m^2}]$ of the electrochemical reaction j in which species i participates. On the contrary, non-electroactive species must then obey a no-flux condition:

$$-\mathbf{n} \cdot \mathbf{N}_{\mathrm{i}}|_{x=0} = 0 \quad \text{(Eq. 2.10)}$$

Regarding the local current density itself at the surface, it is defined as per the electroanalytical version of the Butler-Volmer equation [8], relating the oxidation and reduction contributions taking place in a single electron transfer between two species:

$$i_{\mathrm{loc,j}}(E(t)) = \mathrm{F}k_{\mathrm{j}}^{0}\left[\exp\left(\frac{(1-\alpha_{\mathrm{j}})\mathrm{F}\left(E(t)-E_{\mathrm{f,j}}^{0}\right)}{\mathrm{R}T}\right)c_{\mathrm{Ox}} - \exp\left(\frac{-\alpha_{\mathrm{j}}\mathrm{F}\left(E(t)-E_{\mathrm{f,j}}^{0}\right)}{\mathrm{R}T}\right)c_{\mathrm{Red}}\right] \quad \text{(Eq. 2.11)}$$

in which k_{j}^{0} $[\mathrm{m/s}]$ is the standard heterogeneous electrochemical rate constant, while $E_{\mathrm{f,j}}^{0}$ $[\mathrm{V}]$ represents the formal potential of said electrochemical reaction, an adjustment of the standard potential E_{j}^{0} for non-ideal conditions. Additionally, α_{j} stands for the cathodic charge transfer coefficient. Moreover, concentrations c_{Ox} and c_{Red}, as they appear in Eq. 2.11, are evaluated at the electrode surface ($x = 0$). Given this formulation, the total current density registered in the CV is at last composed of the sum of the partial currents at the surface, such that:

$$i(E(t)) = \sum_{\mathrm{j}} i_{\mathrm{loc,j}}(E(t)) \quad \text{(Eq. 2.12)}$$

2.2. Results and Discussion

Table 2.1: Fixed parameters for the CV studies, pertaining to the operating conditions and physicochemical properties.

Parameter	Value	Description
$c_{\mathrm{A}}^{\mathrm{bulk}}, c_{\mathrm{X}}^{\mathrm{bulk}}$	$50\ [\mathrm{mol/m^3}]$	Bulk concentrations of reactants A and X
d_{WE}	$2\times10^{-3}\ [\mathrm{m}]$	Diameter of the working electrode (WE)
$E_{\mathrm{v1a}}, E_{\mathrm{v2a}}$	$0, 1.5\ [\mathrm{V}]$	Switching potentials for anodic case
$E_{\mathrm{v1c}}, E_{\mathrm{v2c}}$	$0, -2\ [\mathrm{V}]$	Switching potentials for cathodic case
v	$0.05\ [\mathrm{V/s}]$	CV scan rate
D	$1.33\times10^{-9}\ [\mathrm{m^2/s}]$	Diffusion coefficient of all species

Having made explicit the theoretical framework and necessary assumptions informing the CV model, the following parameters in Table 2.1 were fixed, so as to constitute basic and expectable CV operating conditions, as well as the species' physicochemical properties. These remain constant throughout the subsequent studies, in which various cyclic voltammograms were simulated via COMSOL Multiphysics.

Firstly, one may analyse how the kinetic and thermodynamic parameters directly influence the current density response of the system. For this purpose, the anodic reaction (EEC) was chosen, though an analogue study may be performed in the counter-reaction. In studying the varying effects of the standard heterogeneous rate constants k_{j}^{0} or homogeneous first-order rate constant k_{j} of a given reaction j, it is pertinent to resort to CV-specific dimensionless numbers that relate said values with respect to the diffusion coefficient D and/or the assumed scan rate v. As such, the following dimensionless numbers are respectively used [9]:

$$\Lambda_{\mathrm{j}} = k_{\mathrm{j}}^{0}\sqrt{\frac{\mathrm{R}T}{\nu_{\mathrm{e,j}}\mathrm{F}Dv}} = \begin{cases} \Lambda_{\mathrm{j}} \geq 15\ (\mathrm{reversible}) \\ 15 > \Lambda_{\mathrm{j}} > 10^{-2(1+\alpha_{\mathrm{j}})}\ (\mathrm{quasi-reversible}) \\ \Lambda_{\mathrm{j}} \leq 10^{-2(1+\alpha_{\mathrm{j}})}\ (\mathrm{irreversible}) \end{cases} \qquad \text{(Eq. 2.13)}$$

$$\lambda_{\mathrm{j}} = \frac{k_{j}\mathrm{R}T}{v\mathrm{F}} \qquad \text{(Eq. 2.14)}$$

such that the former pertains to an electron transfer reaction (E step), while the latter to a chemical one (C step). As shown in Eq. 2.13, the evaluation of Λ_{j} with respect to the cathodic charge transfer coefficient α_{j} allows for the assessment of the reaction's reversibility. On the other hand, α_{j} itself, being dimensionless, does not require a new formulation. Considering all this, the results present in Fig. 2.2 exhibit the parametric sweep of the electrochemical and chemical kinetic parameters of the anodic case, as well as a variation of $E_{\mathrm{f,a,2}}^{0}$, thus varying its thermodynamic favourability with respect to the first electron transfer, characterized by $E_{\mathrm{f,a,2}}^{0}$.

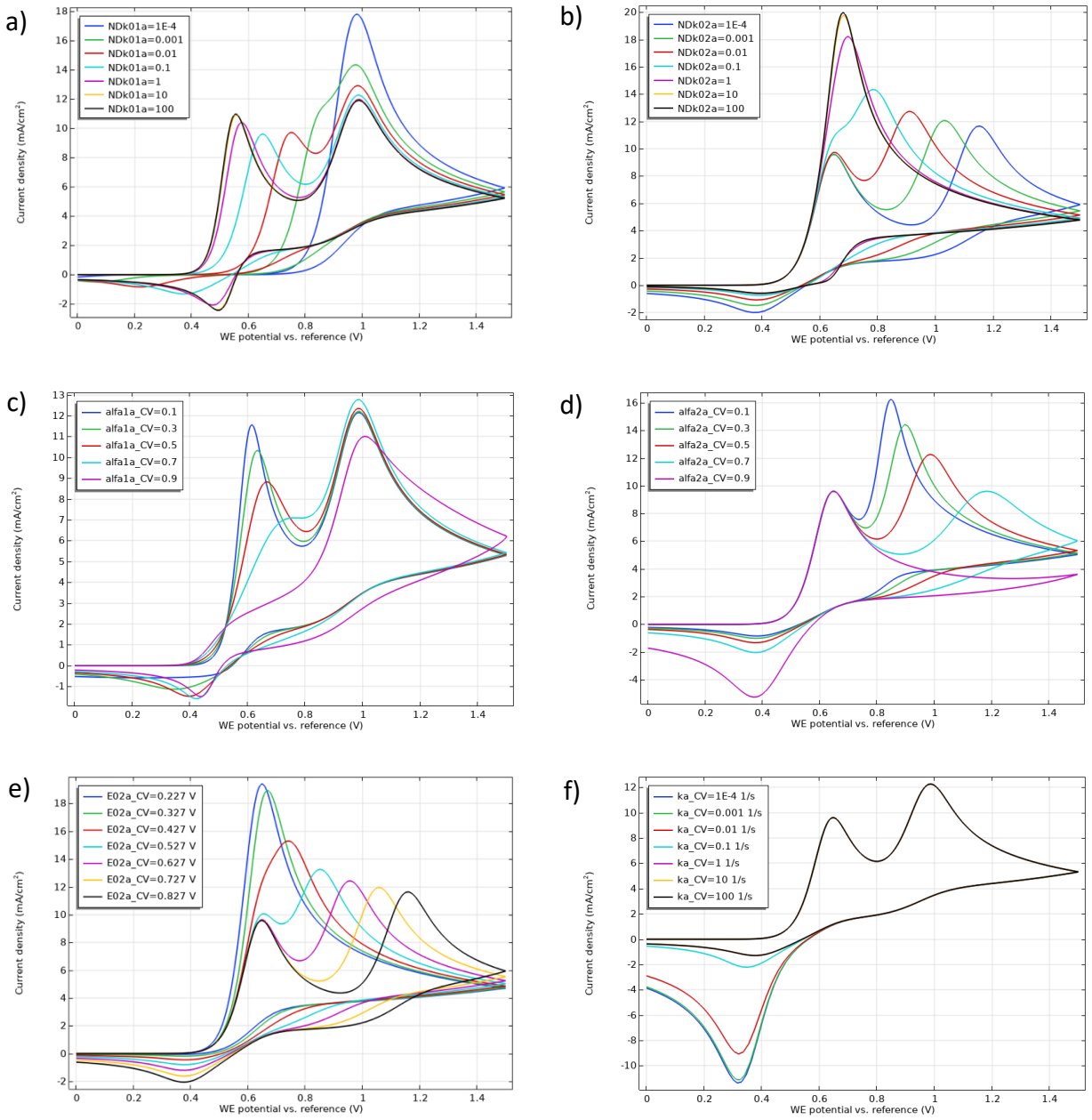

Figure 2.2: Parametric sweep of CV for anodic case (EEC), with all legends listing the values in ascending order; a) varying the dimensionless heterogeneous rate constant of the first E step (Eq. 2.13), $\Lambda_{a,1}$; b) and for the second E step, $\Lambda_{a,2}$; c) varying the cathodic charge transfer coefficient of the first E step, $\alpha_{a,1}$ (affecting Eq. 2.11); d) and for the

second E step, $\alpha_{a,2}$; e) varying the formal oxidation potential of the second E step, $E^0_{f,a,2}$ (affecting Eq. 2.11), while fixing $E^0_{f,a,1}$; f) varying the dimensionless homogeneous rate constant of the C step, $\lambda_{a,1}$ (Eq. 2.14); in all sub-figures, the non-varying parameters are fixed according to Table 2.2, while operating conditions and physicochemical properties are expressed in Table 2.1.

The anodic reaction's parametric sweeps reveal the many ways in which a mechanism can manifest through its kinetic and thermodynamic constants in a CV. By varying $\Lambda_{a,1}$ and $\Lambda_{a,2}$ from irreversible to reversible, Fig. 2.2.a) and 2.2.b) respectively evidence how the distinction of each current density peak in the oxidation sweep of the CV (of potentials $E_{p_{ox},a,1}$ and $E_{p_{ox},a,2}$, one for each E step) is dependent on the magnitude of their exchange current densities (see Eq. 3.16). The increased reversibility of the first E step in Fig. 2.2.a) sets $E_{p_{ox},a,1}$ apart from $E_{p_{ox},a,2}$ and towards lower potentials, while simultaneously increasing its reduction peak's current density magnitude and shifting its potential, such that the difference between $E_{p_{ox},a,1}$ and $E_{p_{red},a,1}$decreases. Additionally, Fig. 2.2.b) reveals the convolution of the two partial currents, since the change of $\Lambda_{a,2}$ does not exactly affect the kinetics of the first E step but instead overlaps it and increases the current density response, the more reversible it is.

The kinetic analysis is extended to the study of the cathodic charge transfer coefficients $\alpha_{a,1}$and $\alpha_{a,2}$ (Fig. 2.2.c) and 2.2.d), respectively). Being the asymmetry factor which dictates the prevalence of either oxidation or reduction over the other (see Eq. 2.11), its decrease naturally amplifies the oxidation peak of each corresponding E step, while diminishing the reduction peak. This is especially seen in Fig. 2.2.d), in which the higher $\alpha_{a,2}$, the higher $E_{p_{ox},a,2}$ and the lower its corresponding partial peak current density.

Moreover, the effect of varying thermodynamic favourability of the second electron transfer in relation to the first, given when $E^0_{f,a,2} < E^0_{f,a,1}$, is assessed in Fig. 2.2.e). Indeed, it is shown how,

for a formal potential inferior to $E^0_{\mathrm{f,a,1}} = 0.527\ \mathrm{V}$, both electron transfers seem to happen simultaneously and form a single peak, giving the erroneous appearance of a single E step. Lastly, considering the irreversible chemical reaction that concludes the EEC mechanism, Fig. 2.2.f) exhibits how its decreasing rate (influenced by $\lambda_{\mathrm{a},1}$) greatly increases the magnitude of the reduction peak current density of the first E step, while having no influence on the second.

Having performed the parametric sweep, providing an insight into the behaviour of the prescribed mechanism of the anodic reaction, specific values were assigned to the thermodynamic and kinetic parameters of both reactions (Table 2.2), thus characterising both mechanisms. Parameters' values are adapted from [6] in order to assure experimental consistency. The corresponding reversibility of each electron transfer is furthermore assessed in Table 2.3.

Table 2.2: Fixed parameters for the CV studies, pertaining to the operating conditions and physicochemical properties.

Parameter	Value	Description
$E^0_{\mathrm{f,a,1}}, E^0_{\mathrm{f,a,2}}$	$0.527, 0.657\ [\mathrm{V}]$	Formal potentials of anodic reactions
$k^0_{\mathrm{a,1}}, k^0_{\mathrm{a,2}}$	5.3×10^{-6}, $1.2 \times 10^{-7}\ [\mathrm{m/s}]$	Standard heterogeneous rate constants of anodic reactions
$\alpha_{\mathrm{a,1}}, \alpha_{\mathrm{a,2}}$	$0.4, 0.5$	Cathodic charge transfer coefficients of anodic reactions
k_{a}	$0.3\ [\mathrm{s^{-1}}]$	Homogeneous first-order rate constant of anodic reaction
$E^0_{\mathrm{f,c,1}}, E^0_{\mathrm{f,c,2}}$	$-0.83, -1\ [\mathrm{V}]$	Formal potentials of cathodic reactions
$k^0_{\mathrm{c,1}}, k^0_{\mathrm{c,2}}$	3.4×10^{-8}, $7.5 \times 10^{-10}\ [\mathrm{m/s}]$	Standard heterogeneous rate constants of cathodic reactions
$\alpha_{\mathrm{c,1}}, \alpha_{\mathrm{c,2}}$	$0.6, 0.7$	Cathodic charge transfer coefficients of cathodic reactions
k_{c}	$1.5 \times 10^{-2}\ [\mathrm{s^{-1}}]$	Homogeneous first-order rate constant of cathodic reaction

Table 2.3: Dimensionless electrochemical rate constants (Eq. 2.13), using the fixed values of Tables 2.1 and 2.2.

Dimensionless number	Value	$10^{-2(1+\alpha_i)}$	Reversibility
$\Lambda_{a,1}$	1.03×10^{-1}	1.58×10^{-3}	Quasi-reversible
$\Lambda_{a,2}$	2.34×10^{-3}	1×10^{-3}	Quasi-reversible
$\Lambda_{c,1}$	6.62×10^{-4}	6.31×10^{-4}	Quasi-reversible
$\Lambda_{c,2}$	1.46×10^{-5}	3.98×10^{-4}	Irreversible

In order to study the simulated voltammograms resulting from Table 2.2, each of the species' concentrations c_i and the 1D domain's length x are respectively non-dimensionalised as follows:

$$c_i^* = \frac{c_i}{c_{A/X}^{bulk}} \quad \text{(Eq. 2.15)}$$

$$x^* = \frac{x}{L} \quad \text{(Eq. 2.16)}$$

in which x^*, depending on L, is therefore dependent on the scan rate v (as per Eq. 2.3). This dependency could pose a problem of incommensurability between simulations at different scan rates, for which another dimensionless length would be required, yet it suffices for the present case of a fixed v.

Taking this into account, Fig. 2.3 presents the CV-related simulations for the anodic case (EEC), while Fig. 2.4 exhibits the cathodic case (ECE). The evaluation of the surface concentrations for both reactions is of special interest. Figure 2.3.c), when paired with the simulated CV in Fig. 2.3.b) and the potential profile of Fig. 2.3.a) of the anodic case, shows the transition from the kinetically-controlled to the diffusion-controlled region in the forward/oxidation sweep (for $t = [0, 30]$ s). In this transition, the concentration of reactant A fully depletes at $x = 0$ and the current density response becomes entirely dependent on the species' diffusion to the surface from the bulk.

Simultaneously, as expected, product D^{2+} is formed via the homogeneous chemical reaction, consuming C^{2+}. A more interesting case is observed for the cathodic counter-reaction in Fig. 2.4.c), in which the surface concentration of Z^{-} depletes completely along with X in the diffusion-controlled region of the backward/reduction sweep. The consistency of the simulated CV results in their expected mechanistic behaviour, when backed by the presented graphs, conclude the accurate definition of physically meaningful dummy reactions to be modelled in flow.

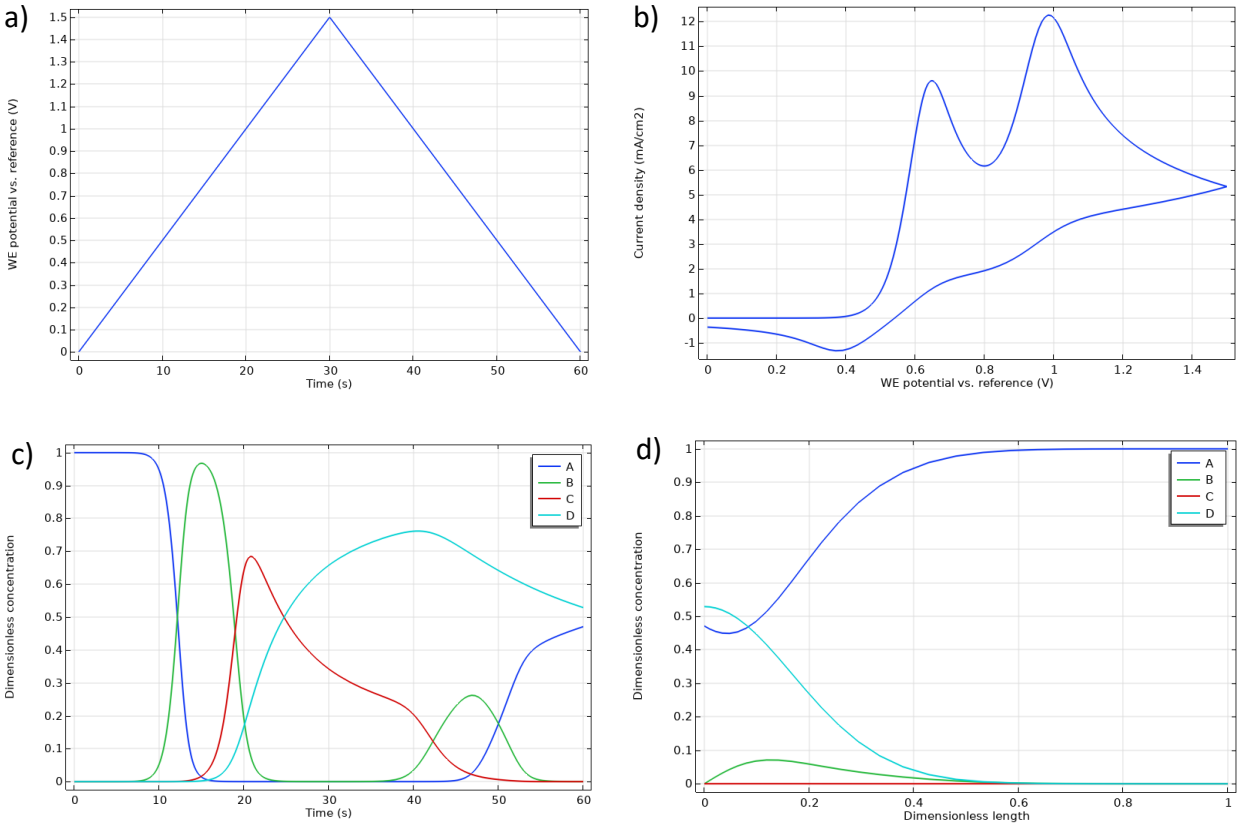

Figure 2.3: Simulated CV-related results for the anodic reaction (EEC), with letters A to D signifying each species, as defined in Section 1; a) sweeping WE potential vs. reference, over time, as determined by Eq. 2.2; b) corresponding CV, as given by Eq. 2.12, showing the current-voltage response; c) time-evolution of the surface concentrations ($x = 0$) during the simulated experiment; d) species' concentrations over the dimensionless length x^*, at $t = t_{\max}$.

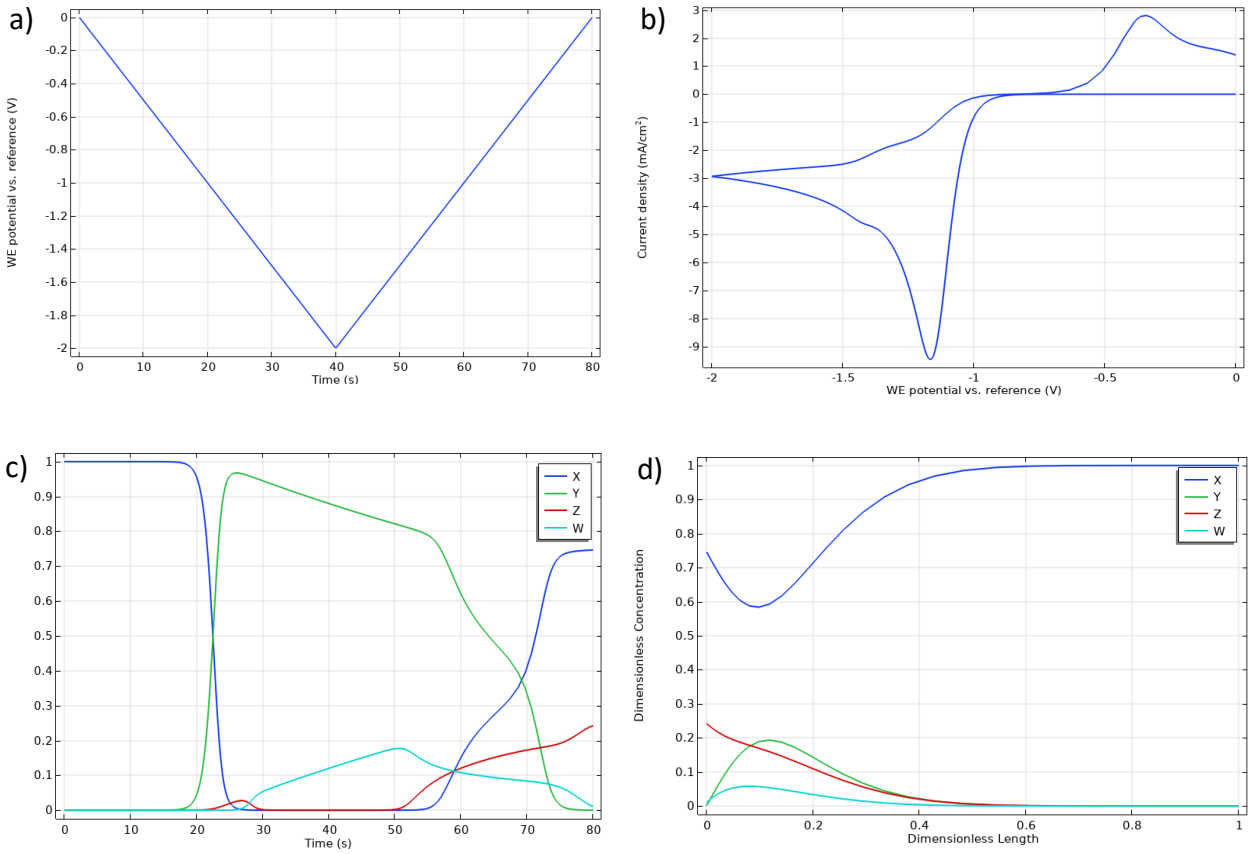

Figure 2.4: Simulated CV-related for the cathodic reaction (ECE), with letters X to Z signifying each species, as defined in Section 1; a) sweeping WE potential vs. reference, over time, as determined by Eq. 2.2; b) corresponding CV, as given by Eq. 2.12, showing the current-voltage response; c) time-evolution of the surface concentrations ($x = 0$) during the simulated experiment; d) species' concentrations over the dimensionless length x^*, at $t = t_{\max}$.

3. 2D Flow Cell Model

Past the appropriate definition and characterization of the reactions in 1D at the electrode-electrolyte interface, the model is further expanded to 2D in accounting for flow cell operating conditions. The adopted single-phase main reaction (anodic, EEC) and counter-reaction (cathodic,

ECE) now occur under fully developed single-pass laminar flow, in an undivided planar parallel plates cell with applied cell potential difference. The medium is assumed buffered, with a supporting electrolyte (e.g. sodium perchlorate, $\mathrm{NaClO_4}$), and all species are considered diluted. The following Subsections elucidate the theoretical framework in which these general conditions come into play.

3.1. Fluid Flow

Assuming the solution to be incompressible, Newtonian and isothermal, its steady-state flow is described by the Navier-Stokes equations of momentum conservation:

$$\rho(\mathbf{u}\cdot\nabla)\mathbf{u} = \nabla\cdot[-p\mathrm{I} + \mu(\nabla\mathbf{u} + (\nabla\mathbf{u})^T)] \qquad \text{(Eq. 3.1)}$$

in which the effect of external forces is neglected, with ρ $[\mathrm{kg/m^3}]$ standing for the fluid density, μ $[\mathrm{Pa}\cdot\mathrm{s}]$ its dynamic viscosity, $\mathbf{u}$ its velocity vector and p the pressure $[\mathrm{Pa}]$. Solving for the latter two variables requires the additional consideration of the incompressible fluid's continuity equation:

$$\nabla\cdot\mathbf{u} = 0 \qquad \text{(Eq. 3.2)}$$

Additionally, boundary conditions need to be imposed at the walls/electrode surfaces, as well as at the inlet and outlet. For the former, one has that, regardless of the surface area being electroactive or not, a no-slip condition is applied to the velocity vector, while the pressure results directly from solving the Navier-Stokes Eq. 3.1 at said boundary:

$$\mathbf{u}|_w = 0 \qquad \text{(Eq. 3.3)}$$

On the other hand, as for the inlet and outlet, the following Table 3.1 summarizes the applied boundary conditions:

Table 3.1: Boundary conditions applied at the inlet and outlet, for the mathematical definition of the fluid flow.

Physics	Pressure	Velocity
Velocity at inlet ($x = 0$)	–	Average velocity $\bar{u}_{\mathrm{in}}$
Pressure at outlet ($x = L$)	Fixed value ($p_{\mathrm{out}} = 0$)	–

Lastly, initial values/guesses for the unidirectional flow velocity profile and the pressure have to be asserted. It suffices to suppose that $\mathbf{u} = (\bar{u}_{\mathrm{in}}, 0)$, while the pressure at the inlet may be estimated via the Hagen-Poiseuille equation for a rectangular channel, considering $p_{\mathrm{out}} = 0\ \mathrm{Pa}$ (Eq. 3.4). Parameters are defined as given in Table 3.2, with L being the flow cell channel's length and s its interelectrode gap.

$$\Delta p = \frac{12\mu L\bar{u}_{\mathrm{in}}}{s^2} \Leftrightarrow p_{\mathrm{in}} = \frac{12\mu L\bar{u}_{\mathrm{in}}}{s^2} \qquad \text{(Eq. 3.4)}$$

As made evident by the formulation of the fluid flow, under a diluted species assumption, the computation of the velocity and pressure profiles is decoupled from the electrochemistry physics itself. This then enables the separate evaluation of $\mathbf{u}$ and p, before considering any electroactive species present in the fluid.

3.2. Mass Transport and Electrochemical Kinetics

Recalling the Nernst-Planck equation given by Eq. 2.4, defining the molar flux of diluted charged particles by diffusion and electrostatic forces, one has that under flow conditions, the flux density of each diluted species i is given by:

$$\mathbf{N}_{\mathrm{i}} = \mathbf{J}_{\mathrm{i}} + \mathbf{u}c_{\mathrm{i}} \Leftrightarrow \mathbf{N}_{\mathrm{i}} = -D_{\mathrm{i}}\nabla c_{\mathrm{i}} - z_{\mathrm{i}}u_{\mathrm{i}}\mathrm{F}c_{\mathrm{i}}\nabla\phi_{\mathrm{l}} + \mathbf{u}c_{\mathrm{i}} \qquad \text{(Eq. 3.5)}$$

such that $\mathbf{u}c_\mathrm{i}$ now defines the advective term. Additionally, on the migrative term, an approximation of the ionic mobility u_i $[\mathrm{m^2 mol/J \cdot s}]$ can be made via the Nernst-Einstein relation, valid at infinite dilution [10]:

$$D_\mathrm{i} = \mathrm{R}Tu_\mathrm{i} \Leftrightarrow u_\mathrm{i} = \frac{D_\mathrm{i}}{\mathrm{R}T} \qquad \text{(Eq. 3.6)}$$

Similarly to previously shown, Eq. 3.5 can then be combined with the steady-state mass-balance of each species for an incompressible single-phase fluid [11]:

$$\frac{\partial c_\mathrm{i}}{\partial t} + \nabla \cdot \mathbf{N}_\mathrm{i} = R_\mathrm{i,j} \Leftrightarrow \frac{\partial c_\mathrm{i}}{\partial t} + \nabla \cdot (\mathbf{J}_\mathrm{i} + \mathbf{u}c_\mathrm{i}) = R_\mathrm{i,j} \Leftrightarrow$$

$$\Leftrightarrow \frac{\partial c_\mathrm{i}}{\partial t} + \nabla \cdot (-D_\mathrm{i}\nabla c_\mathrm{i} - z_\mathrm{i}u_\mathrm{i}\mathrm{F}c_\mathrm{i}\nabla\phi_\mathrm{l} + \mathbf{u}c_\mathrm{i}) = R_\mathrm{i,j} \Leftrightarrow$$

$$\Leftrightarrow \nabla \cdot \left(-D_\mathrm{i}\nabla c_\mathrm{i} - z_\mathrm{i}\frac{D_\mathrm{i}}{\mathrm{R}T}\mathrm{F}c_\mathrm{i}\nabla\phi_\mathrm{l} + \mathbf{u}c_\mathrm{i}\right) = R_\mathrm{i,j} \Leftrightarrow$$

$$\Leftrightarrow \mathbf{u} \cdot \nabla c_\mathrm{i} = \nabla \cdot (D_\mathrm{i}\nabla c_\mathrm{i}) + z_\mathrm{i}\frac{D_i}{\mathrm{R}T}\mathrm{F}c_\mathrm{i}\nabla^2\phi_\mathrm{l} + z_\mathrm{i}\frac{D_\mathrm{i}}{\mathrm{R}T}\mathrm{F}(\nabla c_\mathrm{i} \cdot \nabla\phi_\mathrm{l}) + R_\mathrm{i,j} \qquad \text{(Eq. 3.7)}$$

Moreover, it is assumed that macroscopic electroneutrality is valid in the bulk solution, since the net charge is zero in the inner region of any phase [12]. Significant separation of charge does not take place, so the number of positive and negative charges must balance out:

$$\sum_\mathrm{i} z_\mathrm{i}c_\mathrm{i} = 0 \qquad \text{(Eq. 3.8)}$$

As for boundary conditions, a fixed concentration is specified at the flow cell's inlet, in which the reactants and supporting electrolyte's ionic species (i.e. for A, X, $\mathrm{Na^+}$and $\mathrm{ClO_4^-}$) are defined by:

$$c_\mathrm{i}|_{x=0} = c_{\mathrm{i_{in}}} \qquad \text{(Eq. 3.9)}$$

whereas the remaining intermediate species and products, while non-existent in a real-life setting, are given infinitesimally small concentrations, ε, to ensure numerical stability:

$$c_\mathrm{i}|_{x=0} = \varepsilon \qquad \text{(Eq. 3. 10)}$$

Additionally, no-flux conditions are applied at the electrode surfaces for the non-electroactive species (here $\mathrm{Na^+}$, $\mathrm{ClO_4^-}$ and $\mathrm{D^{2+}}$):

$$-\mathbf{n}\cdot\mathbf{N}_{\mathrm{i}}|_{w}=0 \qquad \text{(Eq. 3.11)}$$

while for the remaining species, all participating in heterogeneous electrochemical reactions, are constituted by the following Neumann boundary conditions, as presented in the CV modelling:

$$-\mathbf{n}\cdot\mathbf{N}_{\mathrm{i}}|_{w}=\frac{-\nu_{\mathrm{i,j}}i_{\mathrm{loc,j}}(\eta_{\mathrm{ref,j}})}{\nu_{\mathrm{e,j}}\mathrm{F}} \qquad \text{(Eq. 3.12)}$$

with the partial local current density at the electrode surfaces $i_{\mathrm{loc,j}}(\eta_{\mathrm{ref,j}})$ $[\mathrm{A/m^2}]$ now being given by a new formulation of the Butler-Volmer equation, known as the "practical" version [8]:

$$i_{\mathrm{loc,j}}(\eta_{\mathrm{ref,j}})=i_{0,\mathrm{ref,j}}\left[\prod_{\nu_{\mathrm{i}}>0}\left(\frac{c_{\mathrm{i}}}{c_{\mathrm{ref}}}\right)^{\nu_{\mathrm{i}}}\exp\left(\frac{(1-\alpha_{\mathrm{j}})\mathrm{F}\eta_{\mathrm{ref,j}}}{\mathrm{R}T}\right)-\prod_{\nu_{\mathrm{i}}<0}\left(\frac{c_{\mathrm{i}}}{c_{\mathrm{ref}}}\right)^{-\nu_{\mathrm{i}}}\exp\left(\frac{-\alpha_{\mathrm{j}}\mathrm{F}\eta_{\mathrm{ref,j}}}{\mathrm{R}T}\right)\right] \qquad \text{(Eq. 3.13)}$$

with ν_{i} being the stoichiometric coefficient of species i, as per the convention of a single electrochemical reaction involving ν_{e} electrons:

$$\underbrace{\sum|\nu_{\mathrm{Ox}}|\mathrm{Ox}}_{\nu_{\mathrm{Ox}}<0}+\nu_{\mathrm{e}}e^{-}\rightleftharpoons\underbrace{\sum|\nu_{\mathrm{Red}}|\mathrm{Red}}_{\nu_{\mathrm{Red}}>0} \qquad \text{(Eq. 3.14)}$$

Eq. 3.13 is furthermore dependent on specific reference conditions, given by c_{ref} $[\mathrm{mol/m^3}]$, involved in the definition of the reference overpotential, $\eta_{\mathrm{ref,j}}$ $[\mathrm{V}]$ (Eq. 3.15). $E_{\mathrm{eq,ref,j}}$ stands for the Nernst equilibrium potential, while variables ϕ_{s} and ϕ_{l} $[\mathrm{V}]$ constitute the electrostatic potential of a given electrode and the electrolyte, respectively.

$$\eta_{\mathrm{ref,j}}=E-E_{\mathrm{eq,ref,j}}=(\phi_{\mathrm{s}}-\phi_{\mathrm{l}})-\left[E^{0}_{\mathrm{f,j}}+\frac{\mathrm{R}T}{\nu_{\mathrm{e,j}}\mathrm{F}}\ln\left(\prod_{\mathrm{i}}\left(\frac{c_{\mathrm{i}}}{c_{\mathrm{ref}}}\right)^{\nu_{\mathrm{i}}}\right)\right] \qquad \text{(Eq. 3.15)}$$

Furthermore, the partial reference exchange current density $i_{0,\mathrm{ref,j}}$ $[\mathrm{A/m^2}]$ is defined as:

$$i_{0,\mathrm{ref,j}}=k^{0}_{\mathrm{j}}\mathrm{F}c_{\mathrm{ref}} \qquad \text{(Eq. 3.16)}$$

As for the current density across the whole solution domain, given by the total sum of the partial current densities (Eq. 3.17), migrative and advective fluxes of the ionic species (thus charge

carrying) need to be accounted for. However, from the electroneutrality assumption (Eq. 3.8), one has that the total current density $\mathbf{i}_\mathrm{l}$ does not depend on the advective term, since:

$$\mathbf{i}_\mathrm{l} = \sum_\mathrm{j} \mathbf{i}_{\mathrm{l,j}} \Leftrightarrow \mathbf{i}_\mathrm{l} = \mathrm{F} \sum_\mathrm{i} z_\mathrm{i} \mathbf{N}_\mathrm{i} \Leftrightarrow$$

$$\Leftrightarrow \mathbf{i}_\mathrm{l} = \mathrm{F} \sum_\mathrm{i} z_\mathrm{i} \mathbf{J}_\mathrm{i} + \mathrm{F}\mathbf{u} \sum_\mathrm{i} z_\mathrm{i} c_\mathrm{i} \Leftrightarrow$$

$$\Leftrightarrow \mathbf{i}_\mathrm{l} = \mathrm{F} \sum_\mathrm{i} z_\mathrm{i} \mathbf{J}_\mathrm{i} \Leftrightarrow \mathbf{i}_\mathrm{l} = \mathrm{F} \sum_\mathrm{i} \left(-z_\mathrm{i} D_\mathrm{i} \nabla c_\mathrm{i} - z_\mathrm{i}^2 \frac{D_\mathrm{i}}{\mathrm{R}T} \mathrm{F} c_\mathrm{i} \nabla \phi_\mathrm{l} \right) \qquad \text{(Eq. 3.17)}$$

Consequently, one may describe the law of conservation of charge as:

$$\nabla \cdot \mathbf{i}_\mathrm{l} = 0 \Leftrightarrow \nabla \cdot (\kappa \nabla \phi_\mathrm{l}) + \mathrm{F} \sum_\mathrm{i} z_\mathrm{i} \nabla \cdot (D_\mathrm{i} \nabla c_\mathrm{i}) = 0 \qquad \text{(Eq. 3.18)}$$

in which κ, the electrical conductivity $[\mathrm{S/m}]$ of the solution, is given by:

$$\kappa = \mathrm{F}^2 \sum_\mathrm{i} z_\mathrm{i}^2 \frac{D_\mathrm{i}}{\mathrm{R}T} c_\mathrm{i} \qquad \text{(Eq. 3.19)}$$

Lastly, the applied cell potential difference U_cell $[\mathrm{V}]$ is thoroughly defined. In this implementation, the cathode was considered the electric ground, such that its electrostatic potential $\phi_\mathrm{s,c}$ is defined as null, and thus to define U_cell is essentially to define the potential at the anode, $\phi_\mathrm{s,a}$. The composition of the potential difference is then as follows:

$$U_\mathrm{cell} = \phi_\mathrm{s,c} - \phi_\mathrm{s,a} \Leftrightarrow U_\mathrm{cell} = 0 - \phi_\mathrm{s,a} \Leftrightarrow$$

$$\Leftrightarrow \phi_\mathrm{s,a} = -U_\mathrm{OCV} + |\eta_\mathrm{ohmic}| + \left| \sum_\mathrm{j} \eta_\mathrm{act,a,j} \right| + \left| \sum_\mathrm{j} \eta_\mathrm{act,c,j} \right| +$$

$$+ \left| \sum_\mathrm{j} \eta_\mathrm{conc,a,j} \right| + \left| \sum_\mathrm{j} \eta_\mathrm{conc,c,j} \right| \qquad \text{(Eq. 3.20)}$$

being defined by: the open circuit voltage U_OCV, the potential for which the net current is null; the activation overpotentials η_act, from the heterogeneous electrochemical reactions at the

surface; the concentration overpotentials η_{conc}; and the overpotential pertaining to the ohmic losses η_{ohmic} [12]. Knowing the solution's electrical conductivity as defined in Eq. 3.19, the latter overpotential is then computed as:

$$|\eta_{\mathrm{ohmic}}| = \left|\frac{i_{\mathrm{l}} s}{\kappa}\right| = \left|\frac{i_{\mathrm{l}} s}{\mathrm{F}^2 \sum_{\mathrm{i}} z_{\mathrm{i}}^2 \frac{D_{\mathrm{i}}}{\mathrm{R}T} c_{\mathrm{i}}}\right| \qquad \text{(Eq. 3.21)}$$

thus finalizing the whole set of constitutive equations for modelling electroorganic synthesis in 2D laminar flow, under tertiary current distribution and the established assumptions. The breakdown of overpotentials as they relate to the applied cell potential difference is exemplified in Fig. 3.1, where a schematic of the flow cell domain with a general reaction and counter-reaction is shown. To avoid numerical instability regarding overlapping boundary conditions, a negligible distance of 2×10^{-3} m (Table 3.2) was given between the inlet and the electrode surfaces.

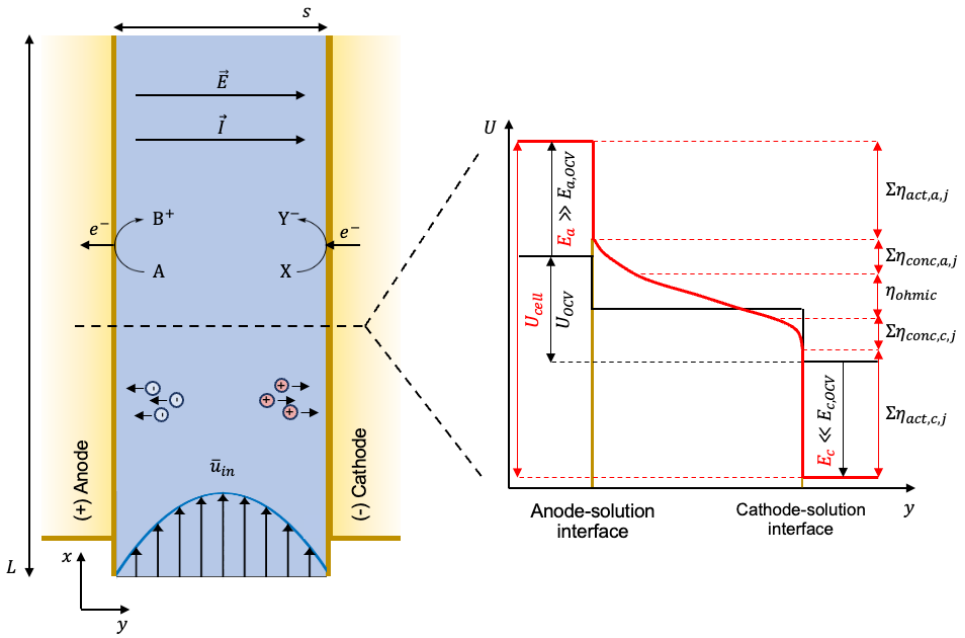

Figure 3.1: Schematic of the 2D model of an undivided planar parallel plates flow cell, under fully developed laminar flow (of average inlet velocity $\bar{u}_{\mathrm{in}}$), and with applied potential difference U_{cell}. On the left, the general movement

of the anions (circles in blue) and the cations (circles in red) is shown, as related to the electrochemical reactions taking place at the anode (oxidation) and cathode (reduction), respectively. On the right, the potential profile, which is dependent on the axial position in the channel length, is here broken down into its overpotentials (Eq. 3.20), for a specific cut line at a certain x. The plot on the right moreover exhibits how the profile (in red) deviates from the initial OCV conditions (in black). The resistivity of the electrode materials is considered negligible, thus not contributing to ohmic losses. Dimensions L and s are as provided in Table 3.2.

3.3. Results and Discussion

Table 3.2: Fixed parameters on the physicochemical properties, operating conditions and geometry of the cell for the modelled electroorganic synthesis in flow.

Parameter	Value	Description
s	4×10^{-3} [m]	Interelectrode gap (given by the gasket's thickness)
L	$2 \times 10^{-3} + 0.1$ [m]	Flow field channel length (with inlet space)
w	5×10^{-2} [m]	Flow field channel width
$\bar{u}_{\mathrm{in}}$	0.15 [m/s]	Average inlet velocity, fully developed flow
ρ	1×10^{3} [kg/m^3]	Fluid density
μ	1×10^{-3} [Pa · s]	Dynamic fluid viscosity
$c_{\mathrm{A_{in}}}, c_{\mathrm{X_{in}}}$	50 [mol/m^3]	Inlet concentrations of A and X
$c_{\mathrm{Na^+_{in}}}, c_{\mathrm{ClO_4^-\,in}}$	100 [mol/m^3]	Inlet concentrations of $\mathrm{Na^+}$ and $\mathrm{ClO_4^-}$
c_{ref}	$c_{A_{in}} = 50$ [mol/m^3]	Reference concentration
ε	1×10^{-10} [mol/m^3]	Artificially small concentration for numerical stability, applied for the inlet concentration of intermediate species
$D_{\mathrm{Na^+}}, D_{\mathrm{ClO_4^-}}$	1.33×10^{-9}, 1.79×10^{-9} [m^2/s]	Diffusion coefficients of supporting electrolyte species (taken from [11])
U_{OCV}	0 [V]	Open circuit voltage

Past the exposition of the theoretical framework and assumptions for the 2D model with tertiary current distribution, the parameters expressed in Table 3.2 were fixed, informing the basic operating conditions and the species' physicochemical properties, as well as the flow cell geometry itself. All other missing parameters regarding the reactions' rate constants and formal potentials were maintained as in Table 2.2, with diffusion coefficients taken from Table 2.1.

As intended, the adopted average inlet flow velocity was such that the flow was laminar and turbulence could be neglected, granting the following Reynolds number:

$$\mathrm{Re} = \frac{\rho \bar{u}_{\mathrm{in}} d_{\mathrm{h}}}{\mu} \Leftrightarrow \mathrm{Re} \approx \frac{\rho \bar{u}_{\mathrm{in}} 2s}{\mu} \Leftrightarrow \mathrm{Re} \approx 1200 \qquad \text{(Eq. 3.22)}$$

For the subsequent simulations, computed once more via COMSOL Multiphysics with physics-controlled meshing, an auxiliary sweep of the applied cell potential difference U_{cell} was required. Starting from the galvanostatically computed U_{OCV}, the steady-state solutions were obtained for potentials from $0\ \mathrm{V}$ (U_{OCV}) to $-3\ \mathrm{V}$, in which the states of the previous computations were sequentially used as the initial values/guesses of the next, thus defining the sweep.

As previously mentioned, the decoupling of the fluid flow from the remaining physics allows for the initial study of the steady-state velocity and pressure profiles obtained from Eq. 3.1 and Eq. 3.2, respectively shown in Fig. 3.2.a) and Fig. 3.2.b). Analysing Fig. 3.2.a), one verifies that the unidirectional parabolic velocity profile is uniform along the axial direction x, expected from the imposition of a two-dimensional fully developed Poiseuille flow at the inlet. Furthermore, the no-slip boundary conditions at the electrode surfaces are also evidenced in Fig. 3.2.a), for which Eq. 3.3 is respected. Additionally, the computation of the pressure scalar field p in Fig. 3.2.b) reveals the gradient driving the flow, with a pressure drop of $11.3\ \mathrm{Pa}$ from the inlet to the outlet.

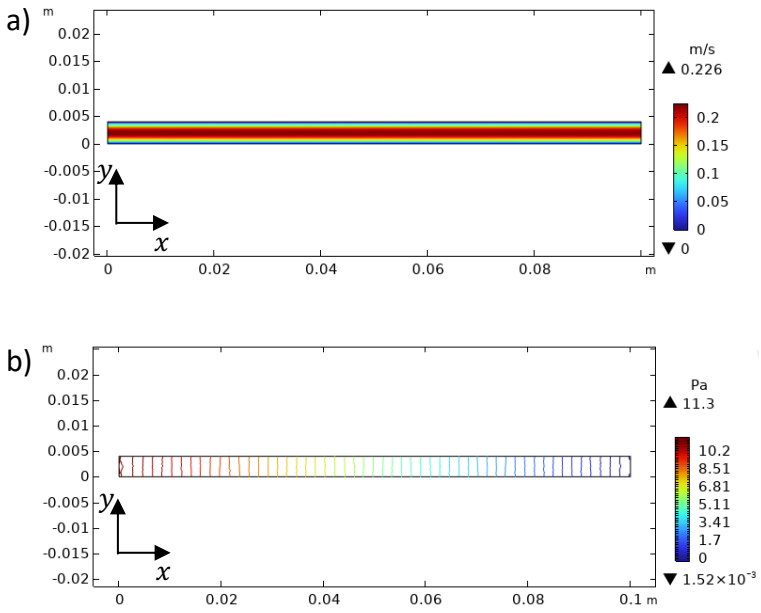

Figure 3.2: Obtained simulated velocity and pressure profiles (sub-plots a) and b), respectively), for fully developed laminar flow, imposed at the inlet with average velocity $\bar{u}_{\mathrm{in}}$. Parameters and dimensions are as provided in Table 3.2, while boundary conditions are expressed in Eq. 3.3 and Table 3.1.

One may now consider the presence of the various species in solution in their generation and consumption, with reactants A and X being continuously fed (along with $\mathrm{NaClO_4}$) at the inlet. The steady-state solution of the coupled equations defined in Subsection 3.2 with an auxiliary sweep thus enables the computation of the electrolyte potential distribution ϕ_{l} in the whole domain, as seen in Fig. 3.3. The graphs allow to conclude that the higher the applied $|U_{\mathrm{cell}}|$, the lower the average ratio $\frac{\phi_{\mathrm{l}}}{|U_{\mathrm{cell}}|}$, while its distribution grows more inhomogeneous. The pronouncement in distribution is particularly salient at the anode surface, where ϕ_{l} becomes dependent on the axial position x (Fig. 3.3.d) and Fig. 3.3.e)). As shall be later shown, these increased gradients are explained by the stronger impact of ohmic losses and concentration overpotentials.

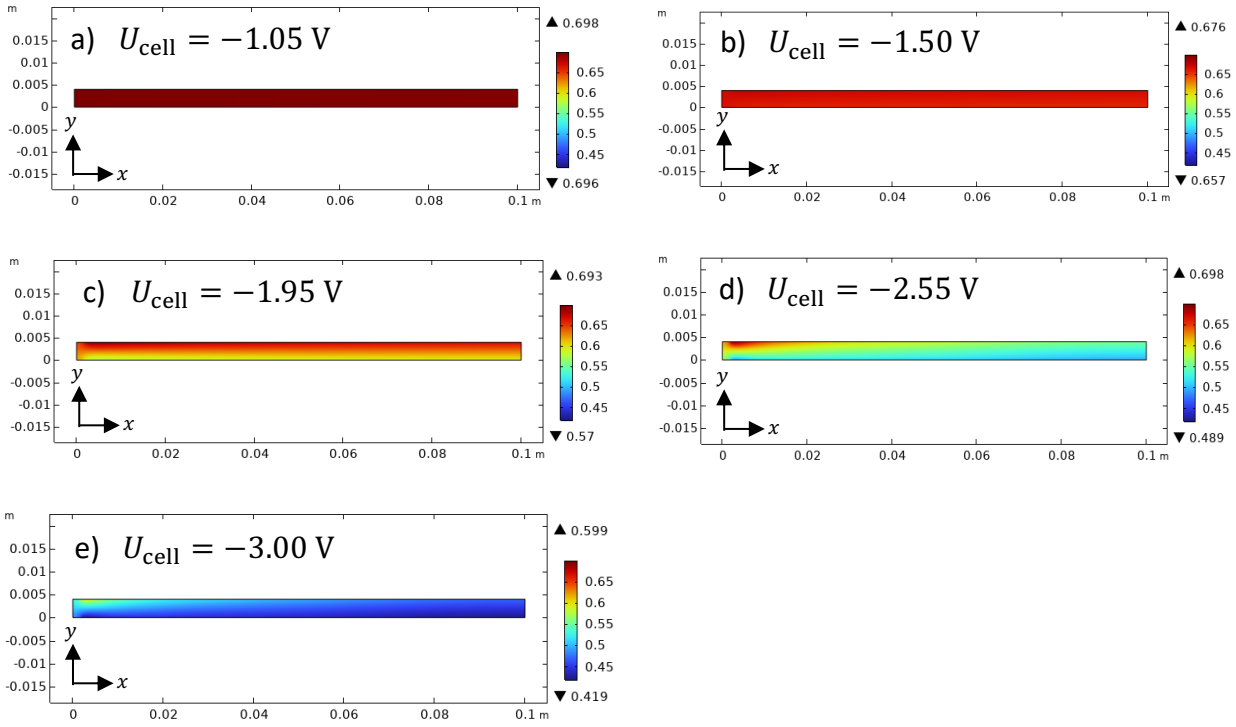

Figure 3.3: Dimensionless electrolyte potential distribution along the flow cell (defined as $\frac{\phi_l}{|U_{cell}|}$, representing the values in each colour bar), for a selection of applied potential differences, U_{cell}. Parameters are as provided in Table 2.1, Table 2.2 and Table 3.2.

In addition, the assessment of the total local current density at the anode surface (Fig. 3.4) grants valuable insight. An increase of its average with $|U_{cell}|$ is registered, reaching limiting conditions for $\phi_{s,a} = 2.55$ V onwards, with a more pronounced gradual decrease along x. One may also observe a heightened finite divergence upon the channel's contact with the electrode surface (i.e. for $x = 2 \times 10^{-3}$ m). The stabilization of the current density into its limiting value for higher potentials is all the clearer via the analysis of the concentrations of reactants A and X at their respective electrode surfaces, depicted in Fig. 3.5. Though both cases exhibit similar concentration profiles for each fixed $\phi_{s,a}$, as per Fig. 3.5.a), reactant A is already fully depleted at the surface for $\phi_{s,a} = 3$ V, unlike X in Fig. 3.5.b). As expected from a higher k^0, the availability of

A at the surface for the first E step is the mass transport-controlled bottleneck that dictates the limiting current density.

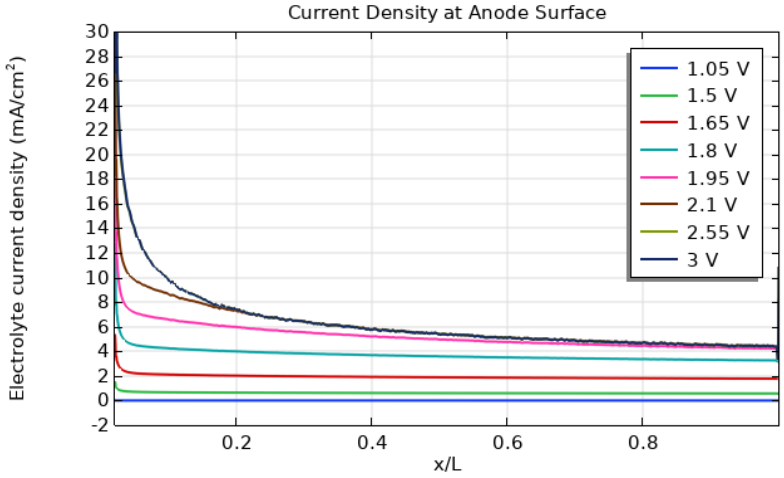

Figure 3.4: Magnitude of local current density i_l (Eq. 3.17) along the dimensionless flow cell length, as registered at the anode surface ($y = s$), for a selection of anode potentials, $\phi_{s,a}$ (in the legend). Parameters are as provided in Table 2.1, Table 2.2 and Table 3.2.

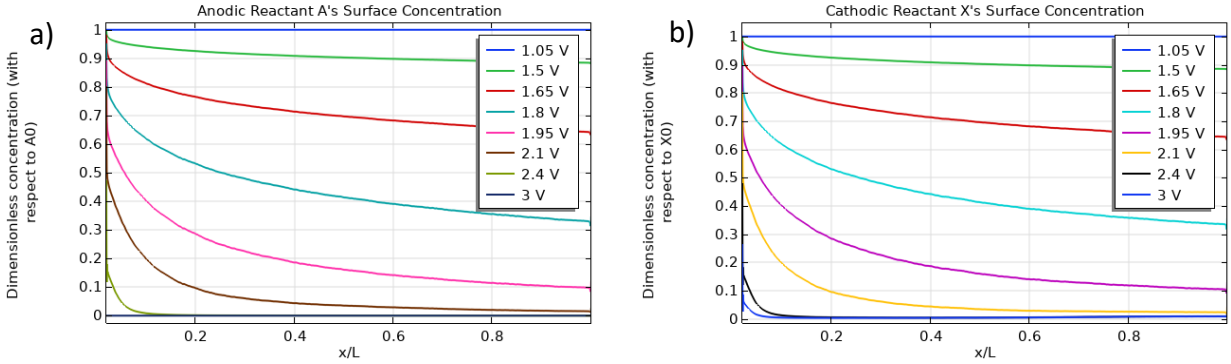

Figure 3.5: Dimensionless reactant concentrations at the electrode surfaces for the anodic case (a), for reactant species A evaluated at $y = s$) and cathodic case (b), for reactant species X evaluated at $y = 0$), along the dimensionless flow cell length, for various anode potentials, $\phi_{s,a}$ (in the legends). Parameters are as provided in Table 2.1, Table 2.2 and Table 3.2.

However, as shown in Fig. 3.4, the reached limiting current density isn't locally equal across the whole axial direction/channel length x, being higher the closer one is to the flow cell inlet.

Studying at various cut lines (Fig. 3.6), this variation, as well as the heightened divergence at $x = 2 \times 10^{-3}$ m in Fig. 3.4, is consistent with the concentration gradient of reactant A along the interelectrode gap s. Indeed, considering Eq. 3.17, Fig. 3.6 exhibits how a decreasing gradient ∇c_{A} along x directly impacts the local limiting current. Conversely, its Nernst linear diffusion layer thickness δ_{A} increases along y.

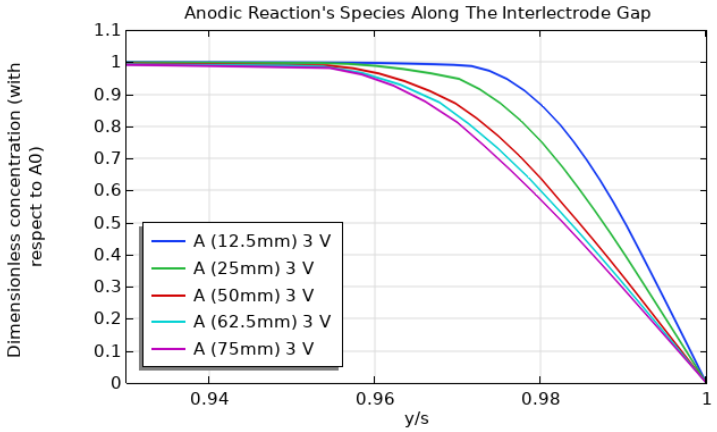

Figure 3.6: Dimensionless concentration profile of reactant species A *at different axial positions* x *along the flow cell channel's length (in the legend, in ascending order), for the maximum anode electrostatic potential,* $\phi_{\mathrm{s,a}} = 3$ V. *Parameters are as provided in Table 2.1, Table 2.2 and Table 3.2.*

Having simulated the electroorganic synthesis in flow for various applied potential cell differences, one is also able to obtain a polarization plot as shown in Fig. 3.7. In it, it is evident how the acceptable operating range for an average inlet velocity of $\bar{u}_{\mathrm{in}} = 0.15$ m/s is $1.20 \text{ V} < |U_{\mathrm{cell}}| < 2.55$ V. Indeed, for $|U_{\mathrm{cell}}| \leq 1.20$ V the average current density is close to null, while its limiting value is reached for $|U_{\mathrm{cell}}| \geq 2.55$ V at $i_{\mathrm{avg,lim}} = 6.38 \text{ mA/cm}^2$. Furthermore, recalling Eq. 3.20, there is a direct relation between these U_{cell} intervals and the domination of each type of overpotential. As seen in Fig. 3.7, the activation overpotentials η_{act} dominate at lower i_{avg}, with the solution's ohmic drop increasing along $|U_{\mathrm{cell}}|$, leading to a region in which the concentration overpotentials η_{conc} exhibit higher influence. Lastly, since the average limiting current density is reached when the system becomes fully mass transport-controlled (previously

depicted in Fig. 3.4), it could be further increased via a higher flow rate, for which the convective fluxes would increase, affecting the polarization plot and delaying this divergence towards higher values of $|U_{\text{cell}}|$.

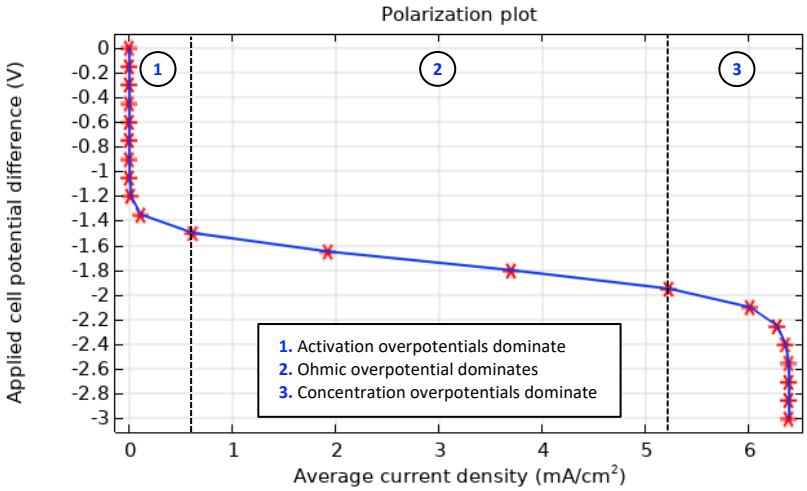

Figure 3.7: Interpolated polarization plot, depicting the obtained average magnitude of the current density i_{avg} corresponding to each simulated potential cell difference U_{cell}. The plot is further divided into three sections of overpotential dominance (in the legend), as related to Eq. 3.20. Parameters are as provided in Table 2.1, Table 2.2 and Table 3.2.

4. Conclusion

The understanding of complex multi-transfer electroorganic synthesis in its kinetics and mass transport is enhanced via mathematical modelling of its interconnected physics. In seeking to exhibit this, a general modelling framework was developed for a dummy reaction, pertinent for fostering collaborative work within the MiEl network. The chosen case study pertained to an EEC anodic reaction and an ECE cathodic counter-reaction, both specifically devised in this work.

Its main reactivities were first successfully analysed via 1D CV modelling, with respect to pertinent dimensionless numbers. Moreover, in the expounding of its theoretical groundwork, all necessary

assumptions were clarified and related to its corollary equations, enabling an informed interpretation of the obtained simulated concentration and current-potential profiles. By assigning physically meaningful parameters, this initial step was crucial in the verification of the implementation of the reactions' mechanisms, before adaptation to flow.

Following on the CV model, the 2D model was then theoretically formulated. Assuming a tertiary current distribution and operating in an undivided planar parallel plates flow cell under laminar regime, the system was evaluated for a wide range of applied cell potential differences. The COMSOL Multiphysics implementation of its coupled physics enabled the computation of distributions of electrolyte potential, concentrations and current density along the flow cell's domain. Furthermore, limiting cases were studied in their relation to dominating overpotentials, assessing the cell's operability range via a polarization plot. In summary, the final continuum scale 2D flow cell model constitutes a solid foundation exhibiting the applicability of mathematical modelling in extracting necessary insight into the synthesis itself and its operating conditions, thus achieving the deliverable's main objective successfully.

5. Outlook

Though the basic modelling foundation has been asserted in this deliverable, there remain several crucial physics/operating conditions to be modelled, looking to align with standard electroorganic syntheses in flow, as well as meeting MiEl's doctoral candidates' experimental set-ups. For this purpose, the following modelling challenges are still to be met, providing a general roadmap of future work: **1)** two-phase flow, tackling gas evolution reaction as occurring at the electrode surfaces; **2)** turbulent flow, resorting to either Large Eddy Simulation (LES) or Reynolds-averaged Navier-Stokes (RANS) methodologies for 3D modelling; **3)** adsorption, thus considering inner-sphere electrochemical processes; **4)** porous electrodes, demanding collaborative work in the

extraction of effective parameters via mesoscale modelling; **5)** concentrated solution assumption, impacting the modelling of the species' mass transport; **6)** and membrane implementation, constituting the reactor as divided.

6. Literature

(1) Schotten, C.; Nicholls, T. P.; Bourne, R. A.; Kapur, N.; Nguyen, B. N.; Willans, C. E. Making Electrochemistry Easily Accessible to the Synthetic Chemist. *Green Chemistry*. 2020. https://doi.org/10.1039/d0gc01247e.

(2) Regnier, M.; Vega, C.; Ioannou, D. I.; Noël, T. Enhancing Electrochemical Reactions in Organic Synthesis: The Impact of Flow Chemistry. *Chem. Soc. Rev.* **2024**, *53* (21), 10741–10760. https://doi.org/10.1039/D4CS00539B.

(3) Savéant, J.; Costentin, C. *Elements of Molecular and Biomolecular Electrochemistry*; 2019. https://doi.org/10.1002/9781119292364.

(4) COMSOL. *COMSOL Multiphysics® v. 6.2*. COMSOL AB, Stockholm, Sweden.

(5) Batchelor-Mcauley, C.; Compton, R. G. Voltammetry of Multi-Electron Electrode Processes of Organic Species. *Journal of Electroanalytical Chemistry* **2012**, *669*. https://doi.org/10.1016/j.jelechem.2012.01.016.

(6) Tapia Mattar, V.; Gavilán-Arriazu, E. M.; Rodriguez, S. A. Study of Electrochemical Mechanisms Using Computational Simulations: Application to Phenol Butylated Hydroxyanisole. *J Chem Educ* **2022**, *99* (2). https://doi.org/10.1021/acs.jchemed.1c01230.

(7) Schön, P.; Krewer, U. Revealing the Complex Sulfur Reduction Mechanism Using Cyclic Voltammetry Simulation. *Electrochim Acta* **2021**, *373*. https://doi.org/10.1016/j.electacta.2020.137523.

(8) Dickinson, E. J. F.; Wain, A. J. The Butler-Volmer Equation in Electrochemical Theory: Origins, Value, and Practical Application. *Journal of Electroanalytical Chemistry* **2020**, *872*. https://doi.org/10.1016/j.jelechem.2020.114145.

(9) Compton, R. G.; Banks, C. E. *Understanding Voltammetry*; 2007. https://doi.org/10.1142/6430.

(10) Bard, Allen J.; Inzelt, G.; Scholz, F. *Electrochemical Dictionary-2nd Edition*; 2012.

(11) Colli, A. N.; Bisang, J. M. Tertiary Current and Potential Distribution Including Laminar/Turbulent Convection, Diffusion, and Migration by the Finite Volume Method Using OpenFOAM. *Ind Eng Chem Res* **2021**, *60* (32). https://doi.org/10.1021/acs.iecr.1c01884.

(12) Fuller, T. F.; Harb, J. N. *Electrochemical Engineering / Thomas F. Fuller, (Georgia Institute of Technology, US), John N. Harb, (Brigham Young University, US)*; 2018; Vol. 1.